Finite-rate chemistry effects in turbulent hypersonic boundary layers: A direct numerical simulation study

D. Passiatore [1,2,*] L. Sciacovelli [2] P. Cinnella [3] and G. Pascazio [1]

[1] *DMMM, Politecnico di Bari, via Re David 200, 70125 Bari, Italy*

[2] *Laboratoire DynFluid, Arts et Métiers ParisTech, 151 Bd. de l'Hôpital, 75013 Paris, France*

[3] *Sorbonne Université, Institut Jean Le Rond d'Alembert, 4 Place Jussieu, 75005 Paris, France*

(Received 18 November 2020; accepted 20 April 2021; published 10 May 2021)

The influence of high-enthalpy effects on hypersonic turbulent boundary layers is investigated by means of direct numerical simulations (DNS). A quasiadiabatic flat-plate air flow at free-stream Mach number equal to 10 is simulated up to fully developed turbulent conditions using a five-species, chemically reacting model. A companion DNS based on a frozen-chemistry assumption is also carried out, in order to isolate the effect of finite-rate chemical reactions and assess their influence on turbulent quantities. In order to reduce uncertainties associated with turbulence generation at the inlet of the computational domain, both simulations are initiated in the laminar flow region and the flow is let to evolve up to the fully turbulent regime. Modal forcing by means of localized suction and blowing is used to trigger laminar-to-turbulent transition. The high temperatures reached in the near-wall region including the viscous and buffer sublayers activate significant dissociation of both oxygen and nitrogen. This modifies in turn the thermodynamic and transport properties of the reacting mixture, affecting the first-order statistics of thermodynamic quantities. Due to the endothermic nature of the chemical reactions in the forward direction, temperature and density fluctuations in the reacting layer are smaller than in the frozen-chemistry flow. However, the first- and second-order statistics of the velocity field are found to be little affected by the chemical reactions under a scaling that accounts for the modified fluid properties. We also observed that the Strong Reynolds Analogy remains well respected despite the severe hypersonic conditions and that the computed skin friction coefficient distributions match well the results of the Renard-Deck decomposition extended to compressible flows.

DOI: 10.1103/PhysRevFluids.6.054604

I. INTRODUCTION

The accurate prediction of turbulent hypersonic flows is a major subject for the design of planetary atmosphere reentry bodies or hypersonic aircrafts. Recently, vehicles concepts involving hypersonic flight are driving renewed attention not only in the defense and military fields, but also in the areas of spatial tourism and transatmospheric flight (a recent review can be found in Ref. [1]). The massive amount of kinetic energy in a hypersonic free stream is converted into internal energy as the gas flows across the bow shock; the high temperatures reached in this regime can cause vibrational excitation and gas dissociation effects that strongly modify the forces and heat transfer acting on the surface. More generally, internal energy relaxation, chemical reactions, and gas-surface interactions can occur in hypersonic flows at rates that are similar to the fluid motion ones, resulting in a nonequilibrium thermochemical state. These processes have a strong

*Corresponding author: donatella.passiatore@poliba.it

effect on aerodynamic performance of reentry objects and may vary global properties of the system [2]; at the same time, heat transfer rates, ablation, and instability growth (which lead to boundary layer transition and breakdown to turbulence) could be altered as well [3]. Such high-temperature effects not only modify the inviscid flow behavior, but also affect turbulence dynamics. Carrying out physical experiments in the working conditions of interest is generally a costly (sometimes infeasible) task [4]; hence the necessity of performing high-fidelity numerical simulations to palliate the lack of experimental data. More specifically, direct numerical simulations (DNS), which ensure the resolution of the whole active range of temporal and spatial scales, represents a powerful tool for a deeper understanding of out-of-equilibrium, high-speed flows and for the development of improved Reynolds-averaged Navier-Stokes (RANS) models. Turbulence models currently employed in hypersonic vehicle design have been developed under perfect-gas assumptions, and their predictive performance for chemically reacting real gas flows is highly uncertain [5].

Significant research effort has been put into linear and non linear boundary layer stability analyses of hypersonic laminar boundary layers, with and without thermochemical nonequilibrium effects (see Refs. [6–13]), since accurate predictions of laminar-to-turbulent transition onset are of crucial importance for the evaluation of aerodynamic and heat transfer coefficients and for the design of the thermal protection system (TPS). Such studies highlighted the existence of multiple modes in the supersonic regime, and the dominant role played by Mack's mode [14], commonly referred to as the second mode. This mode is strongly influenced (destabilized or stabilized) by the thermodynamic properties at the wall [15]. A few studies have investigated the initial stages of transition: for instance, Franko *et al.* [16] assessed the influence of different chemistry models in predicting the second mode growth rate and Marxen *et al.* [10] performed an analysis of the influence of primary and secondary amplitude perturbations, without encompassing transition.

Regarding fully developed turbulence in boundary layer configurations, a handful of high-fidelity DNS studies have been carried out at low-enthalpy, nonreacting conditions. Duan *et al.* [17,18] performed DNS of temporally evolving, zero-pressure-gradient turbulent boundary layers in the high-Mach regime and varying wall temperatures. Mach numbers up to 20 were considered in the work of Lagha *et al.* [19]. A comparative study between low- and high-enthalpy, reactive boundary layers can be found in the work of Duan *et al.* [20], who carried out temporally evolving boundary layer simulations, albeit a moderate temperature value was imposed at the wall ($\approx$2400 K) resulting in weak chemical activity. Recently, more attention has been paid to hypersonic, cold-wall boundary layers in spatially evolving configurations [21,22], but thermodynamic conditions were such that a nonequilibrium thermochemical state is not present. Chemical nonequilibrium in high-enthalpy turbulent boundary layer flows has been extensively studied by Duan and Martín [23,24] at moderate Reynolds numbers, whereas thermal nonequilibrium has been recently investigated on isotropic decaying turbulence [25,26] and mixing layers [27].

The objective of the current paper is to investigate finite-rate chemistry effects in spatially evolving, high-enthalpy boundary layers of hypersonic flows. For that purpose we focus on a configuration widely employed in the past for stability studies of boundary layers [10,16,28–31]. Specifically, we consider a flat plate flow of air, modeled as a five-species mixture, with a free-stream Mach number equal to 10 and a quasiadiabatic wall condition. The resulting wall temperature of approximately 5300K is such that the mixture components undergo strong dissociation and recombination reactions in the near-wall region. The calculation is started in the laminar region, where suction and blowing forcing is introduced to trigger boundary layer instability and transition. The computational domain is sufficiently extended in the streamwise direction to achieve a significant portion of flow characterized by fully turbulent regime. A companion DNS is run at the same free-stream conditions and wall temperature by assuming frozen chemical composition. This allows isolating the contribution of finite-rate chemistry effects by direct comparison of the two simulations.

The paper is structured as follows. The governing equations, the numerical set-up and the flow parameters are described in Sec. II. Numerical results are presented in Sec. III, encompassing the analysis of the transitional zone in the first place and of the turbulent integral and statistical

properties afterwards. The validity of the classical and modified Reynolds analogies are discussed and verified, as well as the skin friction decomposition for boundary layer flows. Lastly, conclusions are drawn in Sec. IV.

II. SIMULATION DETAILS

A. Governing equations

We consider flows governed by the compressible Navier-Stokes equations for multicomponent, chemically reacting gases:

$$\frac{\partial \rho}{\partial t} + \frac{\partial \rho u_j}{\partial x_j} = 0, \tag{1}$$

$$\frac{\partial \rho u_i}{\partial t} + \frac{\partial (\rho u_i u_j + p\delta_{ij})}{\partial x_j} = \frac{\partial \tau_{ij}}{\partial x_j}, \tag{2}$$

$$\frac{\partial \rho E}{\partial t} + \frac{\partial [(\rho E + p)u_j]}{\partial x_j} = \frac{\partial (u_i \tau_{ij} - q_j)}{\partial x_j} - \frac{\partial}{\partial x_j}\left(\sum_{n=1}^{\mathrm{NS}} \rho_n u_{n,j}^D h_n\right), \tag{3}$$

$$\frac{\partial \rho_n}{\partial t} + \frac{\partial (\rho_n u_j)}{\partial x_j} = -\frac{\partial \rho_n u_{n,j}^D}{\partial x_j} + \dot{\omega}_n \quad (n = 1, \ldots, \mathrm{NS} - 1). \tag{4}$$

In the preceding equations, ρ_n is the density of the nth species, $\rho = \sum_{n=1}^{\mathrm{NS}} \rho_n$ is the mixture density, NS is the total number of species, u_i ($i = 1, 2, 3$) are the components of the velocity vector in the direction x_i, p is the pressure, $E = e + \frac{1}{2} u_i u_i$ is the specific total energy of the mixture, $u_{n,j}^D$, h_n, and $\dot{\omega}_n$ are the nth species diffusion velocity in the jth direction, specific enthalpy, and rate of production, respectively. τ_{ij} denotes the viscous stress tensor:

$$\tau_{ij} = \mu\left(\frac{\partial u_i}{\partial x_j} + \frac{\partial u_j}{\partial x_i}\right) - \frac{2}{3}\mu \frac{\partial u_k}{\partial x_k}\delta_{ij}, \tag{5}$$

being μ the mixture dynamic viscosity, δ_{ij} the Kronecker symbol and $q_j = -\lambda \frac{\partial T}{\partial x_j}$ represents the heat flux, with λ the mixture thermal conductivity and T the temperature.

Air is modeled as a five-species mixture of N_2, O_2, NO, O, and N. Species' conservation equations are written for NS − 1 species, the NS-th species' partial density being computed as $\rho_{\mathrm{NS}} = \rho - \sum_{n=1}^{\mathrm{NS}-1} \rho_n$. In the following simulations, the NS-th species is chosen to be Nitrogen due to its large mass fraction throughout the computational domain. Each species is assumed to behave as a perfect gas; based on Dalton's law, the mixture pressure equation of state writes:

$$p = \sum_{n=1}^{\mathrm{NS}} p_n = \mathcal{R}\rho T \sum_{n=1}^{\mathrm{NS}} \frac{Y_n}{W_n} = T \sum_{n=1}^{\mathrm{NS}} \rho_n R_n, \tag{6}$$

with Y_n, W_n, and R_n the mass fraction, molecular weight, and gas constant of the nth species, respectively, and $\mathcal{R} = 8.314\,\mathrm{J/mol\,K}$ the universal constant of gases. The thermodynamic properties of high-T air species are computed considering the contributions of translational, rotational and vibrational modes [32]; specifically, the internal energy reads:

$$e = \sum_{n=1}^{\mathrm{NS}} Y_n h_n - \frac{p}{\rho}, \tag{7}$$

with $h_n = h_{f,n}^0 + \int_{T_{\mathrm{ref}}}^{T} (c_{p,n}^{\mathrm{tr}} + c_{p,n}^{\mathrm{rot}}) dT' + e_n^{\mathrm{vib}}$ the nth species enthalpy. Here $h_{f,n}^0$ is the nth species enthalpy of formation at the reference temperature ($T_{\mathrm{ref}} = 298.15\,\mathrm{K}$), $c_{p,n}^{\mathrm{tr}}$ and $c_{p,n}^{\mathrm{rot}}$ the translational

and rotational contributions to the isobaric heat capacity of the nth species, computed as

$$c_{p,n}^{\mathrm{tr}} = \frac{5}{2}R_n, \quad c_{p,n}^{\mathrm{rot}} = \begin{cases} R_n & \text{for diatomic species} \\ 0 & \text{for monoatomic species} \end{cases}, \tag{8}$$

and e_n^{vib} the vibrational energy of species n, given by

$$e_n^{\mathrm{vib}} = \begin{cases} \frac{\theta_n R_n}{\exp(\theta_n/T)-1} & \text{for diatomic species} \\ 0 & \text{for monoatomic species} \end{cases} \tag{9}$$

with θ_n the characteristic vibrational temperature of each molecule (equal to 3393 K, 2273 K, and 2739 K for N_2, O_2, and NO, respectively [33]). After the numerical integration of the conservation equations, an iterative Newton-Raphson method is implemented to compute the temperature from the conservative variables.

With regard to the transport coefficients, pure species' viscosity and thermal conductivity are computed using Blottner's model and Eucken's formula, respectively [34]; the corresponding mixture properties are evaluated by means of Wilke's mixing rule. It should be pointed out that, in the range of temperatures spanned by the present calculations ($T \lesssim 5000$ K), these models are in satisfactory agreement with more recent and accurate models (see, e.g., [35–37]). For instance, a comparison with the models implemented in the MUTATION++ library shows that, in the present temperatures range (350 K $< T <$ 5000 K), discrepancies in the viscosity are of the order of 6%. Somewhat higher discrepancies were observed for the thermal conductivity; however, given the pseudo-adiabatic condition at the wall, the heat flux at the wall is nearly zero independently of the model used for the computation of λ.

In Eq. (4) the mass diffusion phenomenon is governed by Fick's law

$$u_{n,j}^{D}\rho_n = -\rho D_n \frac{\partial Y_n}{\partial x_j} + \rho_n \sum_{n=1}^{\mathrm{NS}} D_n \frac{\partial Y_n}{\partial x_j}, \tag{10}$$

where the first term on the r.h.s. represents the effective diffusion velocity and the second one is a mass corrector term, needed in order to satisfy the mass conservation equation when dealing with nonconstant species diffusion coefficients [38,39]. Specifically, D_n is an equivalent diffusion coefficient of species n into the mixture, computed following Hirschfelder's approximation [40] as

$$D_n = \frac{1 - Y_n}{\sum_{\substack{m=1 \\ m \neq n}}^{\mathrm{NS}} \frac{X_n}{D_{mn}}}, \tag{11}$$

where X_n is the nth species' molar fraction and D_{mn} is the binary diffusion coefficient of species m into species n:

$$D_{mn} = \frac{1}{p}\exp(A_{4,mn})T^{[A_{1,mn}(\ln T)^2 + A_{2,mn}\ln T + A_{3,mn}]}, \tag{12}$$

with $A_{1,mn}, \ldots, A_{4,mn}$ curve-fitted coefficients computed as in Gupta *et al.* [41]. Note that more accurate formulations exist for multicomponent diffusion, such as those based on the Stefan-Maxwell equation [35]; however, these models generally imply the rigorous inversion of a linear system of size NS^2 for each evaluation, which rapidly becomes too computationally expensive for DNS of turbulent wall-bounded flows. Furthermore, as shown later in the results section, the species mass fraction gradients assume moderate values in the present simulations because of the slow chemical activity with respect to the fluid motion events; accordingly, diffusion phenomena are mild and Hirschfelder's approximation, representing the best first-order approximation for the diffusion velocity system [38], can be considered an acceptable model.

Concerning the chemical formulation, the five species interact with each other through a 17-reaction mechanism:

$$\begin{aligned}
&\text{R1:} \quad \mathrm{N_2 + M \Longleftrightarrow 2N + M}\\
&\text{R2:} \quad \mathrm{O_2 + M \Longleftrightarrow 2O + M}\\
&\text{R3:} \quad \mathrm{NO + M \Longleftrightarrow N + O + M},\\
&\text{R4:} \quad \mathrm{N_2 + O \Longleftrightarrow NO + N}\\
&\text{R5:} \quad \mathrm{NO + O \Longleftrightarrow N + O_2}
\end{aligned} \tag{13}$$

being M any of the five species considered. The mass rate of production of the nth species is governed by the law of mass action

$$\dot{\omega}_n = W_n \sum_{r=1}^{\mathrm{NR}} (\nu''_{nr} - \nu'_{nr}) \times \left\{ k_{f,r} \prod_{n=1}^{\mathrm{NS}} \left(\frac{\rho Y_n}{W_n} \right)^{\nu'_{nr}} - k_{b,r} \prod_{n=1}^{\mathrm{NS}} \left(\frac{\rho Y_n}{W_n} \right)^{\nu''_{nr}} \right\}, \tag{14}$$

where ν'_{nr} and ν''_{nr} are the stoichiometric coefficients for reactants and products in the rth reaction for the nth species, respectively, and NR is the total number of reactions. $k_{f,r}$ and $k_{b,r}$ are the forward and backward reaction rates of reaction r, modeled according to Arrhenius' law. Further details can be found in the work of Park [42]. There exist more sophisticated models to describe finite-rate chemistry (see Refs. [43,44]), but given the configuration in question and the temperatures range, Park's model was found being suitable.

A frozen-chemistry model is also used for some of the following results. In this case, the source terms in Eq. (4) are simply set to zero and NS = 2, the only species present being N_2 and O_2.

B. Numerical methods

The governing equations are approximated using high-order finite-difference schemes. The convective fluxes are discretized by means of the 10th-order central scheme using 11 points in each direction, whereas standard fourth-order schemes are used for viscous fluxes. A selective 10th-order centered filter, with an amplitude equal to 0.1, is applied sequentially in each direction to provide numerical stability. The numerical discretization is supplemented with a shock-capturing term based on the Localized Artificial Diffusivity (LAD) approach, initially introduced by Cook and Cabot [45] and later extended to multicomponent flows [46]. In the present implementation, only artificial bulk viscosity and thermal conductivity are introduced, with $C_\beta = 0.5$ and $C_\lambda = 0.005$ (further details can be found in Kawai *et al.* [46]), while the artificial shear viscosity and mass diffusion coefficients are set to zero. Time integration is carried out by means of a third-order TVD Runge-Kutta scheme [47].

C. Computational setup and definitions

We simulate two hypersonic, zero-pressure-gradient, spatially evolving boundary layers over a flat plate, in chemical nonequilibrium ("CN" case) and under a frozen-chemistry assumption ("FR" case), respectively. The free-stream conditions are similar to those considered in previous stability studies [6,7,9,10,31], namely, an external Mach number of $M_\infty = 10$, an external Reynolds number per unit length of $\mathrm{Re}_u = 6.6 \times 10^6\ \mathrm{m}^{-1}$, and a free-stream pressure and temperature of $p_\infty = 3596$ Pa and $T_\infty = 350$ K, respectively. The calculations are initiated in the laminar region, where air with standard composition ($Y_{\mathrm{O_2}} = 0.233$ and $Y_{\mathrm{N_2}} = 0.767$) enters the computational domains.

Self-similar profiles of the flow properties, corresponding to a compressible Blasius boundary layer solution under frozen-chemistry assumptions, are prescribed at the computational domain inlet which is located to a distance x_0 from the plate leading edge (not included in the domain). Based on

TABLE I. Boundary layer properties for finite-rate chemistry DNS at five downstream stations. $\mathrm{Re}_x = \rho_\infty u_\infty x/\mu_\infty$ is the Reynolds number based on the distance from the leading edge x; $\mathrm{Re}_\theta = \rho_\infty u_\infty \theta/\mu_\infty$ is the Reynolds number based on the local momentum thickness; $\mathrm{Re}_\theta^{\mathrm{inc}} = \frac{\mu_\infty}{\overline{\mu}_w}\mathrm{Re}_\theta$ is the momentum-thickness-based Reynolds number in the incompressible scaling; and $\mathrm{Re}_\tau = \rho_w u_\tau \delta_{99}/\overline{\mu}_w$ the friction Reynolds number. Δx^+, Δy_{w}^+, Δy_δ^+, and Δz^+ denote the grid size in inner variables in the x-direction, y-direction at the wall and at the boundary layer edge, and in the z-direction, respectively. $\mathrm{Ma}_\tau = u_\tau/c_w$ stands for the friction Mach number and $H = \delta^*/\theta$ is the boundary layer shape factor. The last station, $\hat{x} = 5100$, will be considered in the following for data analysis.

$\hat{x}$	1000	2000	3000	4000	5100
Re_x	5.04×10^6	10.03×10^6	15.04×10^6	20.04×10^6	25.54×10^6
Re_θ	1741	3141	4494	5784	7149
$\mathrm{Re}_\theta^{\mathrm{inc}}$	272	494	705	907	1120
Re_τ	35	89	120	154	185
Δx^+	2.04	2.78	2.58	2.50	2.45
Δy_{w}^+	0.48	0.66	0.61	0.59	0.58
Δy_δ^+	0.73	1.47	1.80	2.15	2.42
Δz^+	1.35	1.83	1.70	1.65	1.61
Ma_τ	0.14	0.17	0.16	0.16	0.15
H	35.6	33.8	34.6	34.9	34.4

the initial displacement thickness δ_{in}^*, we define a dimensionless streamwise coordinate as

$$\hat{x} = (x - x_0)/\delta_{\mathrm{in}}^* \tag{15}$$

that will be used in the following. At the inflow (i.e., $\hat{x} = 0$), the δ_{in}^*-based Reynolds number is set to $\mathrm{Re}_{\delta^*} = 5000$; a sponge layer is applied from $\hat{x} = 0$ to $\hat{x} = 100$ to prevent distortions of the boundary layer similarity profiles. At the plate wall, the adiabatic wall temperature resulting from the similarity solution, $T_w = 5323$ K, is prescribed along with no-slip, noncatalytic conditions. It should be noted that such high values of wall temperature are never reached in practical flight conditions, since aerodynamic heating is somehow mitigated close to the surface. On the other hand, the present configuration permits to build up on the stability studies previously mentioned and provides fundamental data that will be useful in the future for comparison with upcoming DNS including strong wall-cooling effects. Characteristics-based boundary conditions [48] are used at the inflow, outflow, and free-stream boundaries, whereas periodicity is imposed in the spanwise direction. The dimensions of the computational domain are $L_x \times L_y \times L_z = 5200\delta_{\mathrm{in}}^* \times 240\delta_{\mathrm{in}}^* \times 50\pi\delta_{\mathrm{in}}^*$ in the streamwise (x), wall-normal (y), and spanwise (z) directions, respectively; the domain is discretized with $N_x \times N_y \times N_z = 5236 \times 256 \times 240$ points, corresponding to a total of approximately 3.2×10^8 grid points. The grid spacing is uniform in the streamwise and spanwise directions, whereas a grid stretching is applied in the wall-normal direction to ensure fine resolutions near the wall; specifically, the stretching function is

$$\frac{y(j)}{L_y} = (1-\alpha)\left(\frac{j-1}{N_y-1}\right)^3 + \alpha\frac{j-1}{N_y-1}, \tag{16}$$

where $j \in [1, N_y]$ and $\alpha = 0.25$. The same computational grid is used for both the frozen- and finite-rate chemistry DNS; resolutions are reported in Table I for the latter case at several downstream locations in wall viscous units, the viscous length scale being $l_v = \overline{\mu}_w/(\overline{\rho}_w u_\tau)$. Here $\overline{\mu}_w$ and $\overline{\rho}_w$ denote the time- and spanwise-averaged wall values of viscosity and density, and $u_\tau = \sqrt{\overline{\tau}_w/\overline{\rho}_w}$ the friction velocity based on the averaged wall shear stress $\overline{\tau}_w$. The values obtained along the turbulent portion of the domain (with $\Delta x^+ < 2.6$, $\Delta y_w^+ < 0.6$ and $\Delta z^+ < 1.8$ everywhere) denote an excellent spatial resolution; note that similar values were obtained for the frozen-chemistry DNS.

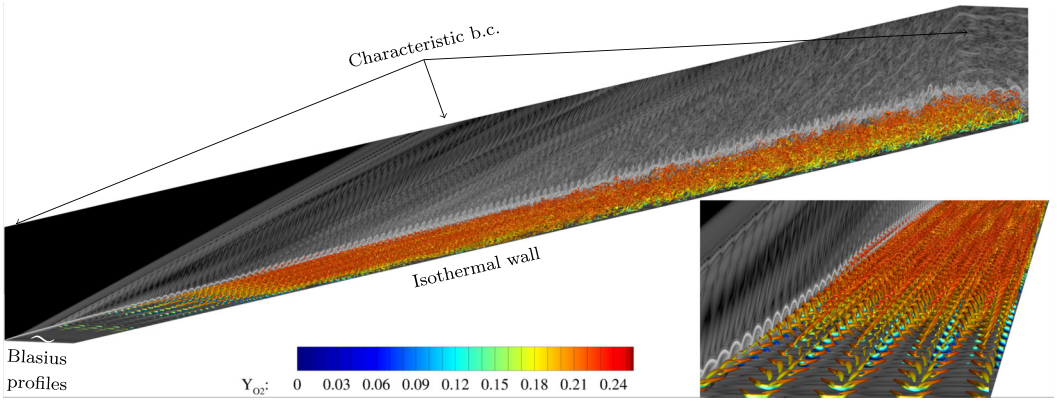

FIG. 1. Isosurfaces of Q-criterion, colored with the local values of O_2 mass fraction for the CN case. The entire computational domain is displayed, along with a zoom on the laminar-to-turbulent transition region.

Additionally, in order to assess the adequacy of the domain size and grid refinement, two-point correlations and one-dimensional kinetic energy spectra are presented in the Appendix.

Transition to turbulence is induced by means of a suction-and-blowing forcing applied at the wall along a spanwise strip located close to the inflow. In this region, a time-and-space-varying vertical velocity is prescribed, corresponding to

$$\frac{v_{\text{wall}}}{u_\infty} = f(x)A\left\{\sin(2\pi\xi - \Omega t) + \cos(4\chi z)\left[0.008\sin\left(2\pi\xi - \Omega t + \frac{\pi}{4}\right) + 1\right]\right\}, \qquad (17)$$

where $\xi = (x - x_{\text{forc}})/L_{\text{forc}}$, $f(x) = \exp(-0.4\xi^2)$ and $\chi = 2\pi/\lambda_z$. The suction-and-blowing forcing is therefore constructed with the superposition of a principal two-dimensional wave and a secondary (lower amplitude) three-dimensional wave with a phase difference. In addition, a stationary (streaky) mode is introduced in order to speed-up flow tridimensionalization and induce an earlier transition. This strategy was found not to impact the fully turbulent region, but to cause large-scale oscillations in the transitional zone, the analysis of which is beyond the scope of the present work. The oscillations are mainly dictated by streaks interaction/destabilization, a mechanism visible in Fig. 3 in the region $1000 < \hat{x} < 2500$. In Eq. (17), x_{forc} and L_{forc} denote the centerline of the forcing strip and its streamwise extent, λ_z the spanwise wavelength, A the forcing amplitude and Ω the dimensional suction-and-blowing frequency. The excitation frequencies and wavelengths are derived from the stability study of Marxen *et al.* [10]. In the present simulations, we set $A = 0.025$, $\Omega = 1.70c_\infty/\delta^*_{\text{in}}$, and $\chi = 0.04/\delta^*_{\text{in}}$, where u_∞ and c_∞ denote the free-stream velocity and speed of sound, respectively. Last, the forcing strip is located at $\hat{x}_{\text{forc}} = 300$ and it extends over $L_{\text{forc}} = 30\delta^*_{\text{in}}$.

A fully turbulent state is achieved at streamwise locations corresponding to a momentum Reynolds number, $\text{Re}_{\theta,\text{tr}}$, approximately equal to 2300 and 2600 for the FR and CN simulations, respectively. In both cases, the fully turbulent region extends over approximately the last third of the computational domain. A global view of the computational domain is given in Fig. 1 showing the boundary conditions, the location of the forcing strip and the fully turbulent domain. A close-up view of the transitional zone is presented in the inset.

In the following, first- and second-order moments of various flow quantities will be presented and discussed; most of the analyses will focus on the turbulent region. For a given variable f, we denote with $\overline{f} = f - f'$ the standard time- and spanwise average, being f' the corresponding fluctuation, whereas $\widetilde{f} = f - f''$ represents the density-weighted Favre averaging, with f'' the Favre fluctuation and $\widetilde{f} = \overline{\rho f}/\overline{\rho}$. Flow statistics are collected for more than four turnover times, after that the initial transient is evacuated and the flow has reached a statistically steady state. The sampling time interval is constant and equal to $\Delta t^+_{\text{stats}} = \Delta t_{\text{stats}} \frac{u_\tau^2}{\overline{\mu}_w/\overline{\rho}_w} = 5.4 \times 10^{-2}$, for a total of ≈70 000 time samples. In

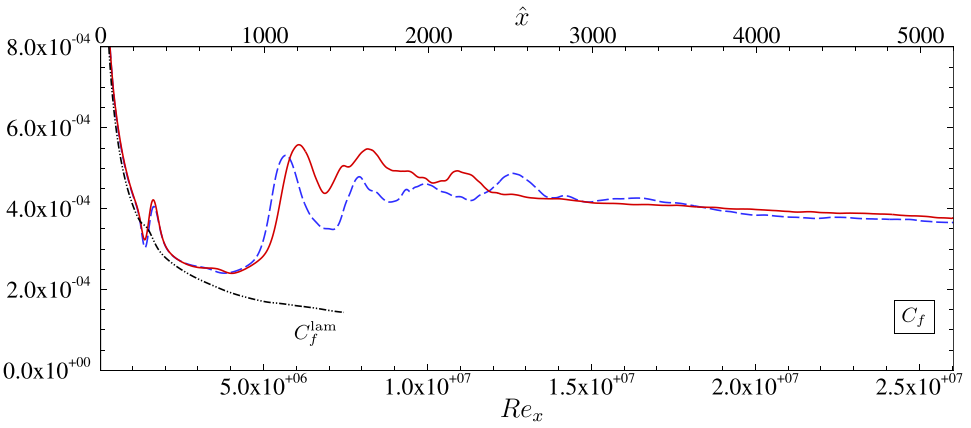

FIG. 2. Wall distributions of the skin friction coefficient C_f as a function of Re_x. (———), CN case; (– – – –), FR case. The black dash-dotted line denotes the laminar correlation C_f^{lam}.

terms of large-eddy timescale, statistics have been collected for a total period of $T_{\mathrm{stats}} u_\tau/\delta_{99} \approx 22$ with a time interval of $\Delta t_{\mathrm{stats}} u_\tau/\delta_{99} = 2.88 \times 10^{-4}$, for both simulations.

III. RESULTS

The streamwise evolution of selected flow properties along the wall is analyzed first. Figure 2 shows the distribution of the skin friction coefficient computed as $C_f = \frac{2\overline{\tau}_w}{\rho_\infty u_\infty^2}$. In the same figure, we also report Blasius' laminar correlation rescaled for compressible boundary layers, $C_f^{\mathrm{lam}} = \frac{0.664}{\sqrt{\mathrm{Re}_x}} \sqrt{\frac{\overline{\rho}_w \overline{\mu}_w}{\rho_\infty \mu_\infty}}$, which is in excellent agreement with the computed C_f up to the suction-and-blowing forcing location. The large temperatures close to the wall lead to a strong friction heating of the boundary layer, and consequently to rather small values of the scaled momentum-thickness Reynolds number $\mathrm{Re}_\theta^{\mathrm{inc}} = \frac{\mu_\infty}{\overline{\mu}_w} \mathrm{Re}_\theta$, in the range [270, 950] for the fully turbulent region. Accordingly, the friction Reynolds number is $\mathrm{Re}_\tau \approx 200$ at the rear end of the plate, as shown in Table I. Despite the very high wall temperature, finite-rate chemistry little affects the skin friction distribution in the laminar and fully turbulent regions, where the chemical nonequilibrium and frozen flow models give very similar results. Significant quantitative discrepancies are observed only in the transition region, albeit the qualitative trends are close by. Figure 3 shows instantaneous

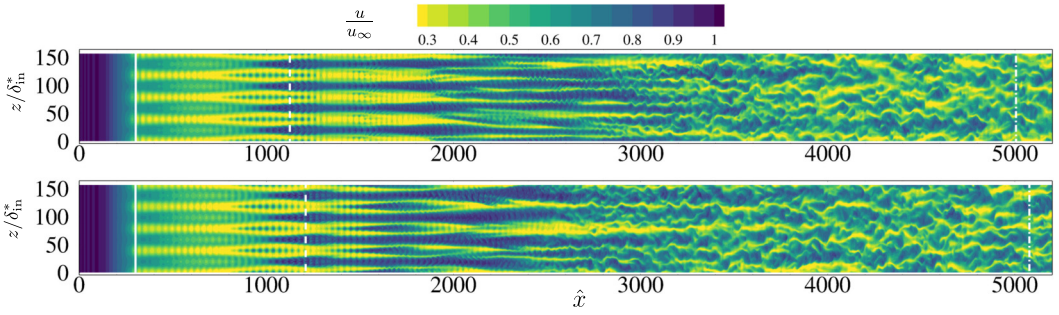

FIG. 3. Instantaneous visualizations of the normalized streamwise velocity in a x-z plane for FR case (top) and CN case (bottom) at $y \approx 4.5\delta_{\mathrm{in}}^*$ (corresponding to $y^+ \approx 30$ at $\hat{x} = 5100$). The spanwise white solid lines denote the blowing-and-suction forcing location; the dashed lines mark the position of the first peak of C_f, and the dash-dot lines indicate the streamwise position at which $\mathrm{Re}_\tau = 185$. The spanwise direction is stretched for better visualization.

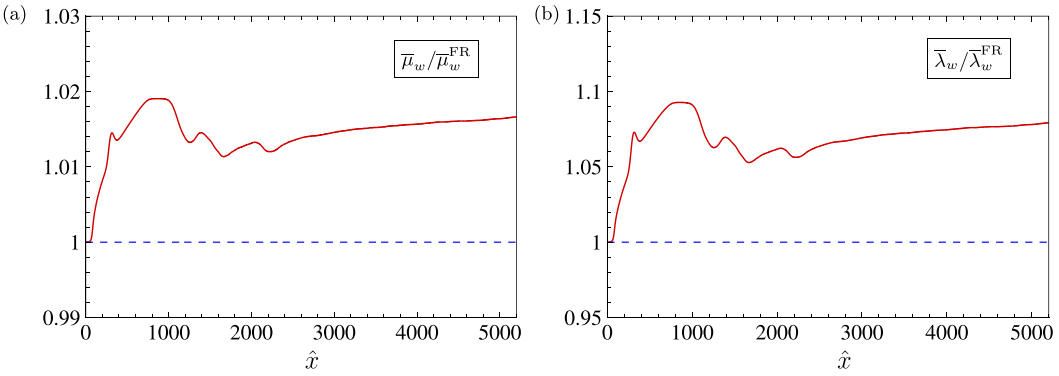

FIG. 4. Streamwise evolution of averaged dynamic viscosity $\overline{\mu}$ (a) and thermal conductivity $\overline{\lambda}$ (b) at the wall, normalized with respect the constant values of the FR case. (———), CN case; (– – – –), FR case.

visualizations of the streamwise velocity in a plane parallel to the wall extracted at $y \approx 4.5\delta^*_{\mathrm{in}}$. Due to the significant spanwise distortion introduced at the forcing point, streamwise vortical structures and streaks are generated immediately downstream, leading to a sudden increase of C_f which deviates from the laminar correlation. Their complex interaction produces a sharp increase of the skin friction and leads to to instabilities growth in the region ranging from $\hat{x} \approx 1000$ to $\hat{x} \approx 2000$, characterized by sinuous streak motions and interactions, and by an oscillatory behavior of the skin friction. The flow finally bursts into turbulence at $\hat{x} \approx 3000$ and relaxes subsequently toward a fully turbulent state. We observe that the initial overshoot is slightly delayed in the CN flow, and fine details of the transitional region are different, both in the instantaneous field and in the average quantities.

Finite-rate chemistry effects alter the mixture composition as the flow evolves along the plate and modify its thermophysical properties, as shown in Figs. 4(a) and 4(b) displaying the streamwise evolution of the averaged molecular viscosity and thermal conductivity along the wall. Unlike the FR case, where the transport properties are uniquely fixed through the imposed wall temperature, for CN these vary according to the evolving local composition, with deviations of the order of 1.5% for the viscosity and 7% for the thermal conductivity. This leads in turn to slightly lower local Reynolds numbers for the chemically reacting case. Both quantities rapidly depart from their inlet values, reaching a peak approximately at the same location where C_f overshoots. The variation of the transport coefficients becomes more smooth in the fully turbulent region, where they gradually increase as a consequence of O_2 dissociation and atomic oxygen formation.

Wall distributions of the averaged species mass fractions for O_2, NO, O, and N are shown in Fig. 5. At the selected flow conditions, dissociation of O_2 (and, to a much smaller extent, of N_2) is quickly activated downstream of the inlet boundary, leading to sudden formation of atomic oxygen and nitric oxide. The amounts of molecular oxygen and nitrogen decrease (and, conversely, increase for the other species) until the location of maximum C_f is reached. The trend is reverted from this point on, due to increased mixing with the external layers. The subsequent series of secondary peaks in the range $\hat{x} \in [1000, 2300]$ are registered roughly in correspondence of those observed in the C_f distribution. For $\hat{x} > 2300$, the chemical composition varies more smoothly moving downstream, indicating that the characteristic chemical timescales are much larger than the local residence flow time. This is confirmed by the increasing amounts of NO, an intermediate product generated by the Zel'dovich mechanism that would be subsequently consumed to produce atomic nitrogen, and by the values of Y_{N}, which remain negligible across the entire flat plate. The separation between the timescales can also be confirmed by comparing the local mixture composition with the equilibrium one. After the breakdown, the average wall pressure is nearly constant and roughly equal to $\overline{p}_w \approx 3060$ Pa. When computing the equilibrium composition at the given T_w and $\overline{p}_w$, the molecular oxygen mass fraction falls down to $Y^{\mathrm{eq}}_{\mathrm{O}_2} \approx 3 \times 10^{-5}$, leading to a large concentration of atomic oxygen, $Y^{\mathrm{eq}}_{\mathrm{O}} \approx 0.23$. Accordingly, one obtains $Y^{\mathrm{eq}}_{\mathrm{N}_2} \approx 0.55$,

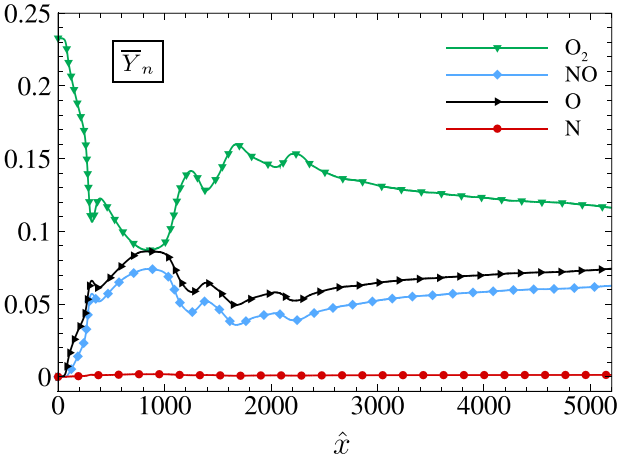

FIG. 5. Streamwise evolution of the averaged mass fractions $\overline{Y}_n$ at the wall for species O_2, NO, O, and N. $\overline{Y}_{N_2}$ is not shown being outside the y-axis bounds.

$Y_{NO}^{eq} \approx 2.8 \times 10^{-3}$ and $Y_N^{eq} \approx 0.21$, which confirms that the local chemical composition shown in Fig. 5 remains everywhere far away from the corresponding equilibrium condition.

In the following, the analysis will focus on the fully turbulent region. Due to the relatively small range of Reynolds numbers covered in the turbulent portion of the computational domain, the nondimensional flow profiles do not vary substantially along the flat plate; therefore, a single streamwise station will be considered for data analysis. Specifically, we examine the station at which $\mathrm{Re}_\tau = 185$ (see Table I), corresponding to $\hat{x} = 5100$ for the CN case and $\hat{x} = 5045$ for the FR case. Unless specified otherwise, wall-normal profiles are plotted in inner scaling, i.e., against the wall coordinate y^+.

A. First-order statistics

Figure 6(a) displays the longitudinal velocity profiles rescaled according to the classical Van Driest transformation

$$u_{VD}^+ = \frac{1}{u_\tau} \int_0^{\overline{u}} \sqrt{\frac{\overline{\rho}}{\overline{\rho}_w}}\, du, \tag{18}$$

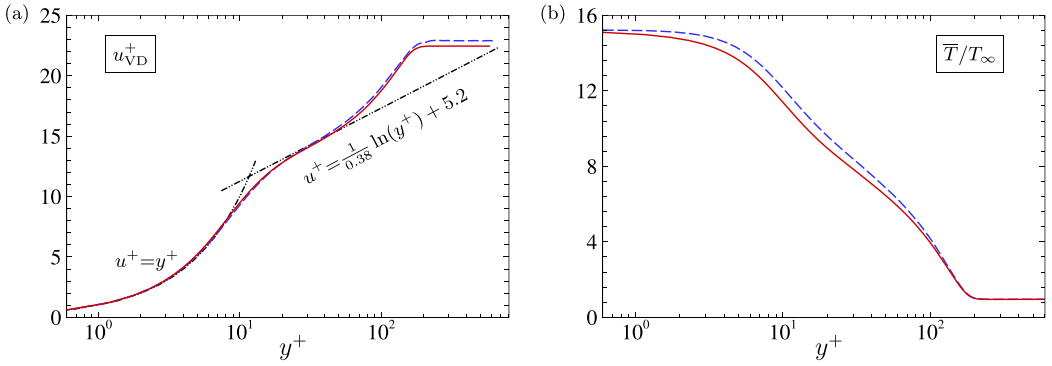

FIG. 6. Wall-normal profiles of the van Driest-transformed streamwise velocity (a) and of the normalized mean temperature (b) at $\mathrm{Re}_\tau = 185$. (——), CN case; (– – –), FR case.

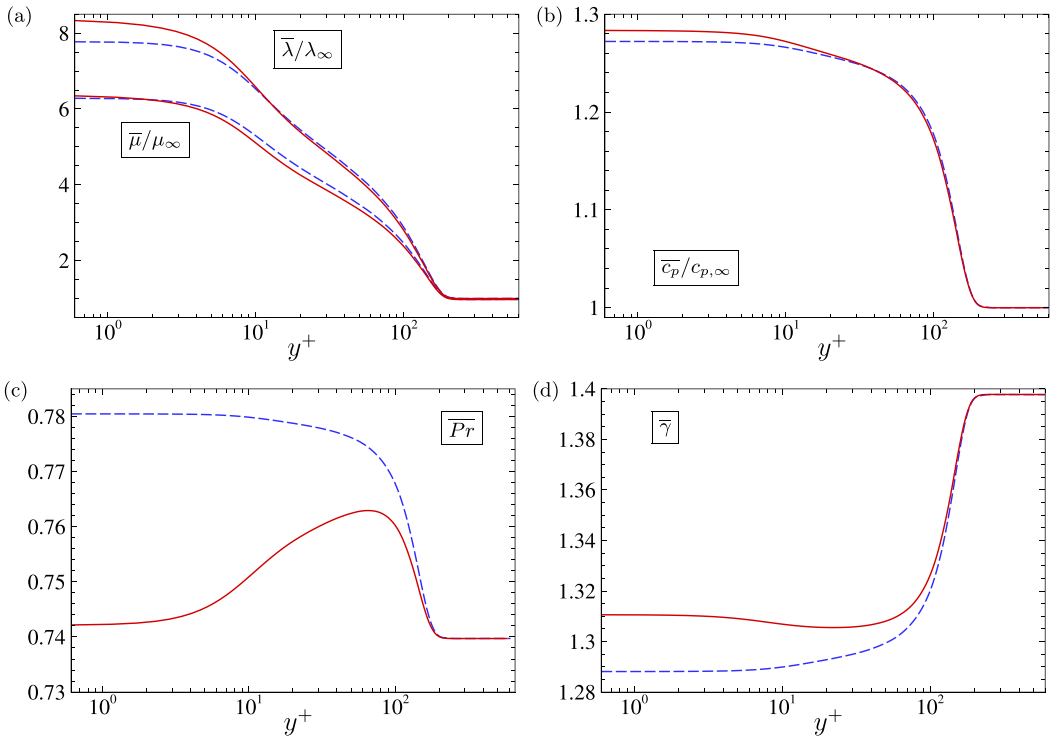

FIG. 7. Wall-normal mean profiles of viscosity and thermal conductivity (a), specific heat capacity at constant pressure (b), Prandtl number (c), and specific heat ratio (d) at $\mathrm{Re}_\tau = 185$. (——), CN case; (- - - -), FR case.

as a function of the inner wall coordinate. The van Driest scaling collapses well velocity profiles for both CN and FR cases in the linear and logarithmic zone; in the outer region the profiles are not perfectly superposed due to the different behavior of $\overline{\tau}_w$ and $\overline{\rho}_w$ which results in slightly different values of u_τ. Of note, the value of the von Kármán constant used in the log law is slightly smaller than the classical one ($\kappa \approx 0.38$, as suggested by Nagib and Chauhanb [49] and Monkewitz [50]), resulting in a more accurate prediction of the slope of the velocity profile in the logarithmic region. The wall-normal mean temperature profiles reported in Fig. 6(b) show that values for the CN boundary layer are below the FR ones by approximately 5% in the buffer region, as an expected consequence of the preponderant endothermic behavior of chemical processes. On the contrary, the mean density profiles (not shown) are not particularly affected by chemical activity.

Wall-normal average distributions of transport properties, Prandtl number $\overline{\mathrm{Pr}} = \overline{\mu c_p/\lambda}$, specific heat capacity $\overline{c_p}$, and specific heat ratio $\overline{\gamma} = \overline{c_p/c_v}$ are shown in Fig. 7. While chemical activity weakly affects the viscosity profile (as discussed before), larger thermal conductivity and isobaric specific heat values (by approximately 6% and 15%, respectively) are observed in the near wall region for the chemically reacting flow compared to the frozen one. These deviations alter the wall-normal profile of $\overline{\mathrm{Pr}}$ (albeit the absolute values never differ by more than 10%), which exhibits a nonmonotonic behavior, with a minimum at the wall and a peak in the logarithmic region. No major differences are observed by comparing $\overline{\mathrm{Pr}}$ and $\overline{\mu}\,\overline{c_p}/\overline{\lambda}$, indicating that that the peculiar behavior of $\overline{\mathrm{Pr}}$ is an effect of the modified mean-flow flow properties and not of the turbulent activity. Finally, changes in chemical composition also lead to minor modifications of the mean specific heat ratio $\overline{\gamma}$ in the inner region of the boundary layer. The latter varies with the temperature in both simulations,

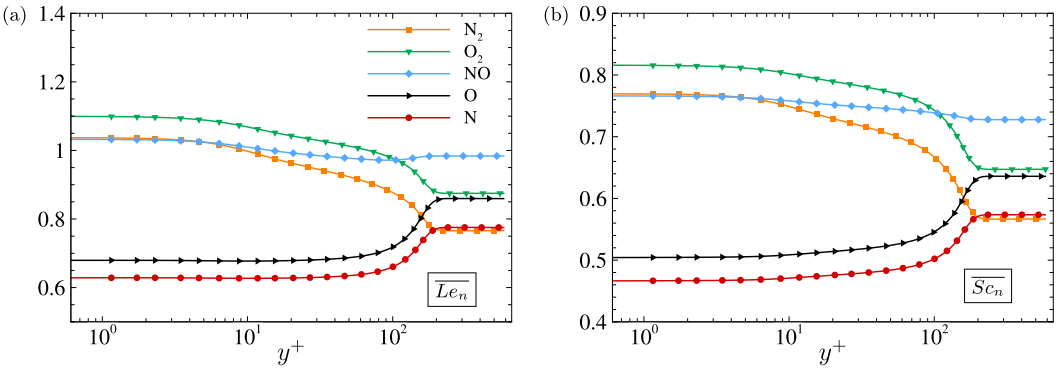

FIG. 8. Wall-normal evolution of mean Lewis number (a) and Schmidt number (b) at $\mathrm{Re}_\tau = 185$, for the chemically reacting simulation, in inner scaling.

deviating from the classical value of 1.4. A larger near-wall value is observed in the reacting flow, also leading to a slightly higher value of the average speed of sound (not shown).

The next series of figures focuses on the behavior of the chemically reacting mixture. Figure 8 shows the wall-normal evolution of the average Lewis and Schmidt numbers for each species, $\overline{\mathrm{Le}_n} = \overline{\lambda/\rho c_p D_n}$ and $\overline{\mathrm{Sc}_n} = \overline{\mu/\rho D_n}$. Larger Lewis numbers indicate that thermal diffusivity effects tend to dominate mass diffusivity; similarly, for higher Schmidt numbers diffusion of momentum dominates mass diffusion. N and O, characterized by higher diffusion coefficients than other species, also exhibit smaller $\overline{\mathrm{Le}}$ and $\overline{\mathrm{Sc}}$ numbers in the reacting near-wall layer, meaning that the two atoms diffuse faster into the rest of the mixture. Moving towards the edge of the boundary layer, both nondimensional coefficients decrease for N_2 and O_2, and increase for the atoms. Overall, variations of $\overline{\mathrm{Le}}$ and $\overline{\mathrm{Sc}}$ across the boundary layer are of the order of 20% for all species except NO, for which the profiles are almost constant; moreover, the local fluctuations amount to less than 1% of the corresponding mean values. We conclude therefore that the use of simplified transport models based on the assumption of constant Le and Sc numbers might constitute an acceptable first approximation, at least for thermodynamic conditions similar to those currently under investigation.

The average profiles of the nth species Damköhler number $\mathrm{Da}_n = \overline{\dot{\omega}_n/\rho}\,\overline{\mu}_w/\overline{\tau}_w$ and mass fraction $\overline{Y_n}$ are reported in Figs. 9(a) and 9(b), respectively. The magnitude of Da_n represents the ratio of the flow characteristic timescale to the chemical timescale, while its positive or negative sign indicates production or depletion of a species, respectively. Note that the present definition of Da_n is based on the characteristic timescale of the inner boundary layer region. The small values observed in Fig. 9(a) imply that chemical reactions are characterized by much longer timescales than the residence time of the flow structures; in other terms, the flow is never too far from frozen-chemistry conditions, even in the near-wall region, justifying the relatively small differences registered between the FR and CN cases. Mass fraction profiles confirm that most of the chemical activity is localized in the viscous sublayer, where O_2 dissociates at a high rate. To quantify the strength of turbulence/chemistry interactions, i.e., the influence of temperature and species mass fractions fluctuations on species production rates, profiles of the species interaction Damköhler number [24] are reported in Fig. 9(c). This quantity, defined as

$$\mathrm{Da}_n^I = \frac{\overline{\omega_n(T,\rho_n)} - \omega_n(\overline{T},\overline{\rho_n})}{\overline{\omega_n(T,\rho_n)}_w}, \tag{19}$$

represents a measure of chemical production due to the turbulent fluctuations in Arrhenius' law, i.e., of the difference $\overline{\omega_n(T,\rho_n)} - \omega_n(\overline{T},\overline{\rho_n}) \neq 0$ due to the nonlinearity of ω_n. Da_n^I takes rather small values across most of the boundary layer, except in the buffer region, where turbulent fluctuations are large enough to generate a significant contribution. Coherently with Fig. 9(a), the species most

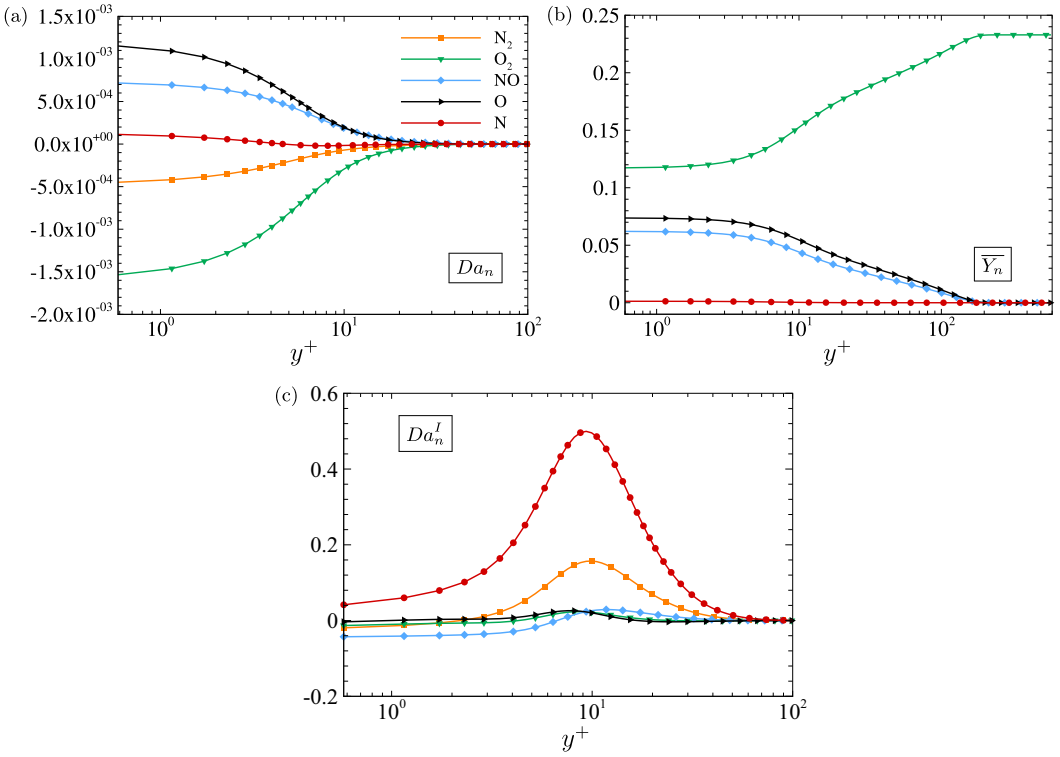

FIG. 9. Wall-normal profiles of the average Damköhler number (a), species mass fractions (b), and species Damköhler number Da_n^I at $\mathrm{Re}_\tau = 185$. In panel (b), N_2 is not shown, being $Y_{N_2} > 0.25$.

affected are the ones with the smaller Da_n (i.e., N and N_2), because of their larger sensitivity to temperature and density fluctuations deriving from turbulent motions. Conversely, the most chemically active species are characterized by small values of Da_n^I, indicating that turbulence/chemistry interactions are somewhat contained in the flow under investigation. A direct consequence is that the evolution of the dynamic quantities is mostly decoupled from that of the chemical species, as discussed in the following by examination of turbulence intensities and energy spectra.

B. Second-order statistics

To further analyze the effect of finite-rate chemistry on turbulent quantities, the wall-normal profiles of Favre-average-based Reynolds stresses are reported in Fig. 10(a). The frozen-flow solution is also reported for reference on the same figure. We observe that finite-rate chemical reactions in the near-wall region partly drain energy from the turbulent fluctuations, which reach a slightly lower peak value of $\overline{\rho u_i'' u_j''}/\overline{\rho}_w u_\tau^2$ in the region of maximum turbulent production. No significant effects are observed for the other Reynolds stress components; a similar behavior has been also registered by Duan *et al.* [20]. Contrary-wise, chemical activity does have an effect on the root mean square (r.m.s.) temperature fluctuations $\sqrt{\overline{T''^2}}/T_\infty$ [reported in Fig. 10(b)], which exhibit a peak value reduced by approximately 10% with respect to the nonreacting case. Interestingly, the location of the largest temperature fluctuations corresponds to a peak in the species fluctuating mass fractions, also located in the buffer layer (Fig. 11), although the near-wall region is hotter.

Averages of unclosed convective and diffusive fluxes arising from Favre averaging of the governing equations were also collected to verify the validity of some common modeling assumptions adopted in lower-fidelity simulations relying on the Reynolds-averaged Navier-Stokes (RANS)

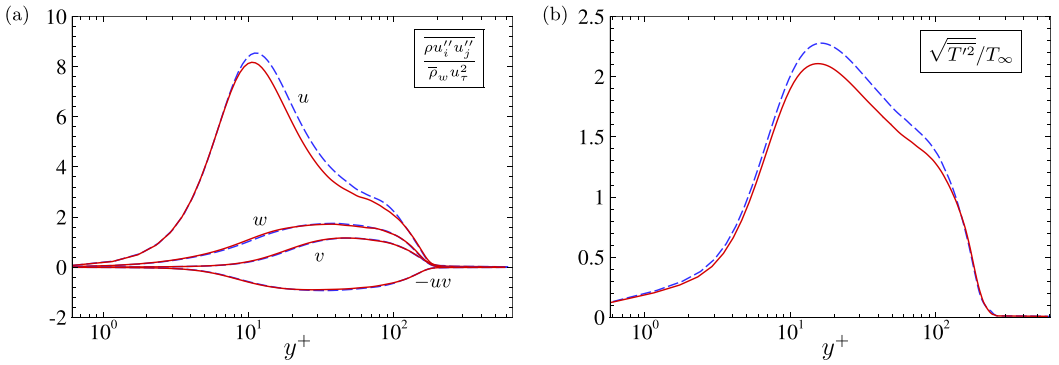

FIG. 10. Wall-normal profiles of Reynolds stresses (a) and of the normalized r.m.s. temperature (b), at $\mathrm{Re}_\tau = 185$. (——), CN case; (- - - -), FR case.

equations. Special focus is put into closures of the turbulent heat transport terms arising in the averaged total energy and species transport equations. By applying a Favre averaging to the total energy equation (3) one obtains

$$\frac{\partial}{\partial t}\left(\overline{\rho}\widetilde{E} + \frac{\overline{\rho u_i'' u_i''}}{2}\right) + \frac{\partial}{\partial x_j}\left[\overline{\rho}\widetilde{u}_j\left(\widetilde{h} + \frac{\widetilde{u}_i\widetilde{u}_i}{2}\right) + \frac{\overline{\rho u_i'' u_j''}}{2}\right]$$
$$= \frac{\partial}{\partial x_j}\left[-\overline{q}_j - \overline{\rho u_j'' h''} + \overline{\tau_{ij} u_i''} - \overline{\rho u_j'' \frac{1}{2} u_i'' u_i''}\right] + \frac{\partial}{\partial x_j}[\widetilde{u}_i(\widetilde{\tau}_{ij} - \overline{\rho u_i'' u_j''})]. \tag{20}$$

It is common practice to model the turbulent transport of a flow property f as a linear function of its average gradient, e.g.,

$$-\overline{\rho u'' f''} = \frac{\mu_t}{C_t}\frac{\partial \widetilde{f}}{\partial x}, \quad -\overline{\rho v'' f''} = \frac{\mu_t}{C_t}\frac{\partial \widetilde{f}}{\partial y}, \quad -\overline{\rho w'' f''} = \frac{\mu_t}{C_t}\frac{\partial \widetilde{f}}{\partial z}, \tag{21}$$

the last term being zero for the present statistically 2D flow. Here μ_t denotes the turbulent viscosity and C_t an *ad hoc* coefficient. The turbulent heat transport terms are usually modeled by introducing

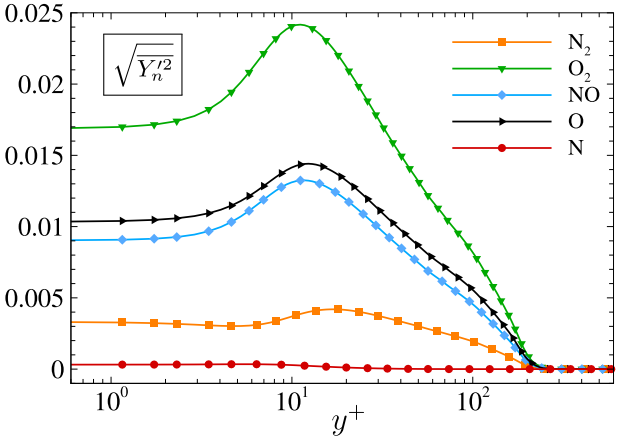

FIG. 11. Wall-normal profiles of r.m.s. mass fractions (b) at $\mathrm{Re}_\tau = 185$ for the CN case.

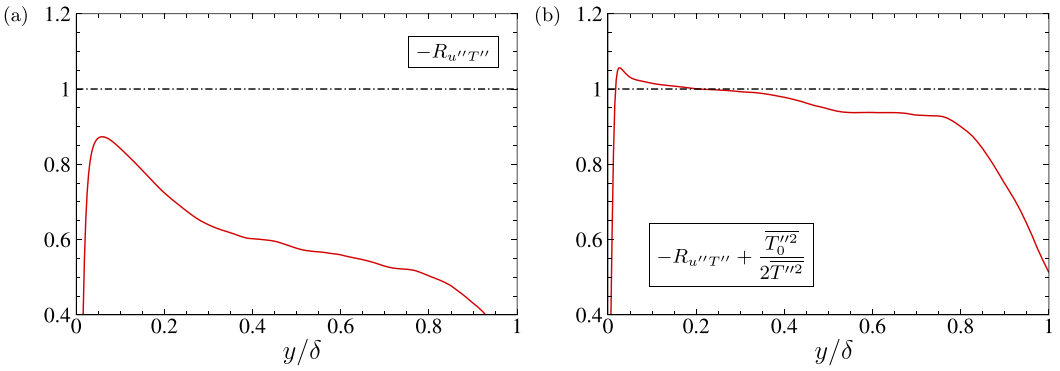

FIG. 12. Correlation coefficient between u'' and T'' without total temperature correction (a) and with total temperature correction (b), at $\mathrm{Re}_\tau = 185$. (———), CN case; (– – –), SRA estimation.

a "turbulent" Prandtl number defined as

$$\mathrm{Pr}_t = \frac{\overline{\rho u'' v''} \partial \widetilde{T}/\partial y}{\overline{\rho v'' T''} \partial \widetilde{u}/\partial y}, \tag{22}$$

which is expected to be approximately equal to 1 throughout the flow, according to the classical so-called Strong Reynolds Analogy (SRA) first discussed by Morkovin [51]. The latter holds under the hypothesis of adiabatic wall, nearly constant total temperature and fully anticorrelated velocity and temperature fluctuations:

$$-R_{u''T''} = -\frac{\overline{u''T''}}{\sqrt{\overline{u''^2}}\sqrt{\overline{T''^2}}} \approx 1. \tag{23}$$

For flows with large total temperature fluctuations (such as in the current case), Eq. (23) is corrected to account for them [52]:

$$-R_{u''T''} + \frac{\overline{T_0''^2}}{2\overline{T''^2}} \approx 1. \tag{24}$$

Figure 12 presents the uncorrected (23) and corrected (24) correlation distributions across the boundary layer, in outer scaling. Clearly, only the corrected correlation approaches reasonably well unity for the present high-enthalpy and high Mach number flow. The assumption is, however, never satisfied in the outer part of the boundary layer, as also found in the work of Duan *et al.* [20]. The turbulent Prandtl number is presented in Fig. 13. For air out of chemical equilibrium, Pr_t follows essentially the trend registered by numerous authors in the literature [17,21,53,54] and is not constant throughout the flow, in contrast with the SRA assumption which predicts $\mathrm{Pr}_t \approx 1$. In the logarithmic and outer layers, Pr_t approaches the value of 0.9, commonly used in turbulence models. A local maximum at about $y^+ = 30$ is observed; in the near-wall region, Pr_t exceeds 1 and becomes singular at the wall due to the quasiadiabatic boundary condition.

Similarly to the procedure followed for the total energy equation, the Favre averaging of the species transport equation (4) leads to

$$\frac{\partial \overline{\rho}\widetilde{Y}_n}{\partial t} + \frac{\partial \left(\overline{\rho}\widetilde{Y}_n \widetilde{u}_j\right)}{\partial x_j} = \frac{\partial}{\partial x_j}\left(\overline{\rho}\widetilde{D}_n \frac{\partial \widetilde{Y}_n}{\partial x_j}\right) + \overline{\rho}\widetilde{\omega}_n \quad + \frac{\partial}{\partial x_j}\overline{\rho u_j'' Y_n''} + \frac{\partial}{\partial x_j}\overline{\rho D_n'' \frac{\partial Y_n''}{\partial x_j}} + \overline{\rho} V_c, \tag{25}$$

where the unclosed terms are the turbulent transport of chemical species, $\frac{\partial}{\partial x_j}\overline{\rho u_j'' Y_n''}$, and the turbulent species diffusion, $\frac{\partial}{\partial x_j}\overline{\rho D_n'' \frac{\partial Y_n''}{\partial x_j}}$. The last term on the r.h.s., $\overline{\rho} V_c$, resulting from Favre averaging of the mass diffusion term in Eq. (10), was found to be negligibly small throughout the flow and

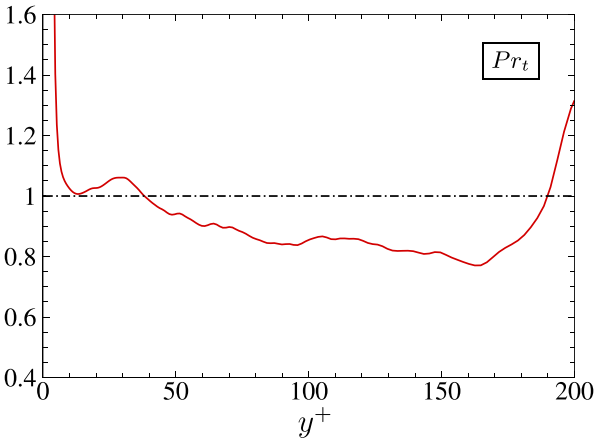

FIG. 13. Wall-normal profiles of the turbulent Prandtl number for CN case, at $\mathrm{Re}_\tau = 185$. (——), CN case; (– – –), SRA estimation.

is not discussed further. The exact turbulent transport and diffusion terms computed from the DNS data are reported in Fig. 14. The turbulent transport of species in the streamwise and wall-normal directions [Figs. 14(a) and 14(b)] are preponderant in the buffer and logarithmic zone. The turbulent diffusion terms along x and y directions [Figs. 14(c) and 14(d)] are one or two orders of magnitude smaller; in particular, $\overline{\rho D_n'' \frac{\partial Y_n''}{\partial x}}$ is active in the region where $\overline{\rho u'' Y_n''}$ peaks, and its contribution can

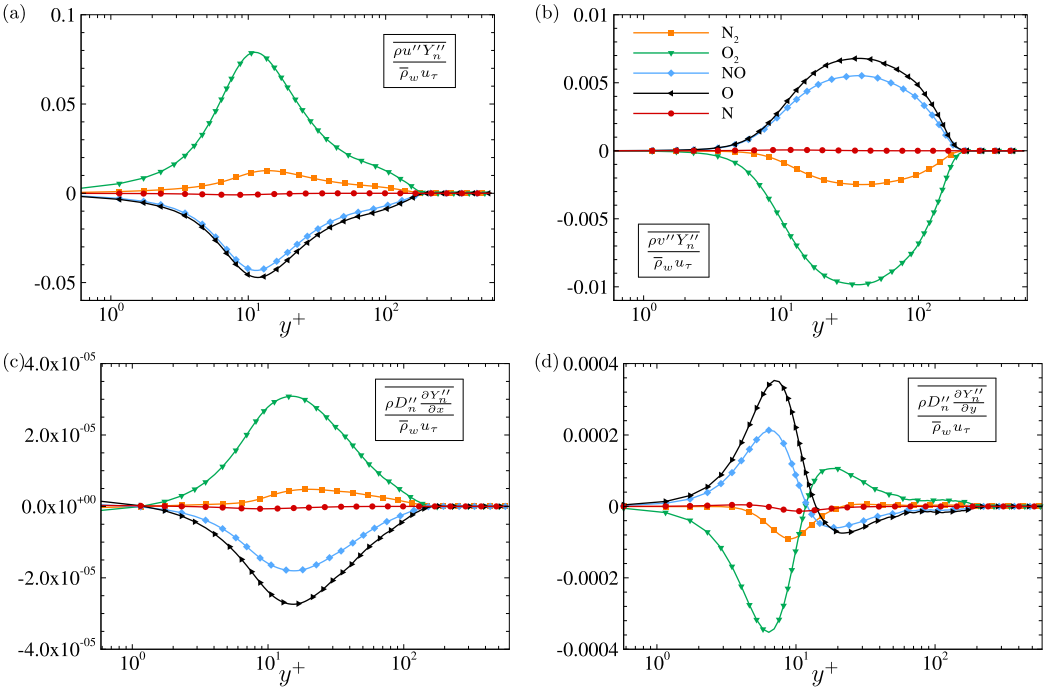

FIG. 14. Normalized turbulent transport of species mass fractions in the streamwise (a) and wall-normal (b) directions; normalized turbulent diffusion fluxes in the streamwise (c) and wall-normal (d) directions, at $\mathrm{Re}_\tau = 185$.

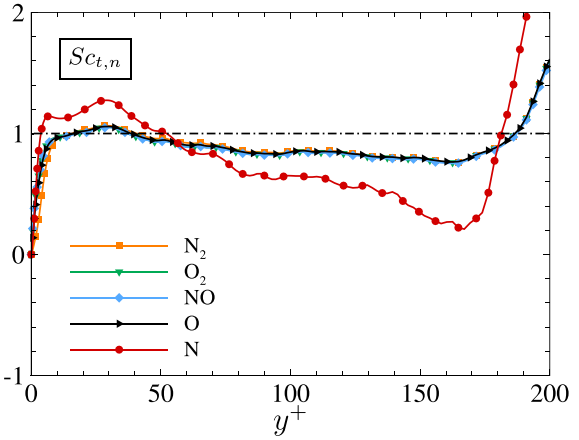

FIG. 15. Wall-normal profiles of the turbulent Schmidt number for CN case, at $\mathrm{Re}_\tau = 185$. The horizontal dashed-dotted line denotes the SRA estimation.

certainly be neglected. However, $\overline{\rho D_n'' \frac{\partial Y_n''}{\partial y}}$ is not completely negligible compared to the other terms in the viscous sublayer and the buffer region, even though, in the RANS approach, the turbulent fluxes deriving from the diffusive terms are not accounted for explicitly.

Likewise the turbulent heat transport fluxes, the species transport fluxes are modeled by introducing a turbulent Schmidt number, e.g.,

$$\mathrm{Sc}_{t,n} = \frac{\overline{\rho u'' v''} \partial \widetilde{Y}_n / \partial y}{\overline{\rho v'' Y_n''} \partial \widetilde{u} / \partial y}, \tag{26}$$

such that

$$-\overline{v'' Y_n''} = \frac{\mu_t}{\mathrm{Sc}_{t,n}} \frac{\partial \widetilde{Y}_n}{\partial y} \tag{27}$$

in the wall normal direction, and similarly for the other directions. Figure 15 reports the $\mathrm{Sc}_{t,n}$ profiles for the five species. In all cases, a value reasonably close to unity (corresponding to the common modeling practice) is observed for all species (except N, characterized by an extremely small species mass flux), in the logarithmic and outer regions of the boundary layer. Such approximation fails in the near-wall region, where $\partial \widetilde{Y}_n / \partial y \approx 0$ due to the noncatalytic boundary condition.

C. Spectral content

To characterize the near-wall turbulent structures, premultiplied spectra of the fluctuating wall-normal and streamwise velocities, as well as of the temperature, are reported in Fig. 16 as a function of the normalized spanwise wave number λ^+. The well-developed spectra indicate that a fully turbulent state has been reached at this position. The spectral content is not significantly altered by chemical effects, and the overall trend is similar to perfect-gas single-species simulations [55]. All of the spectra exhibit a peak in the buffer layer, at the same location were the Reynolds stresses and the temperature fluctuations peak (see Fig. 10).

D. Skin friction analysis

We complete the analysis by studying the contributions of the mean field and turbulent quantities to the generation of skin friction at the plate wall. To this aim, we consider the Renard and Deck [56] decomposition of the mean skin friction in an incompressible boundary layer, extended to compressible boundary layers by Li *et al.* [57]. Based on the kinetic energy transport equation,

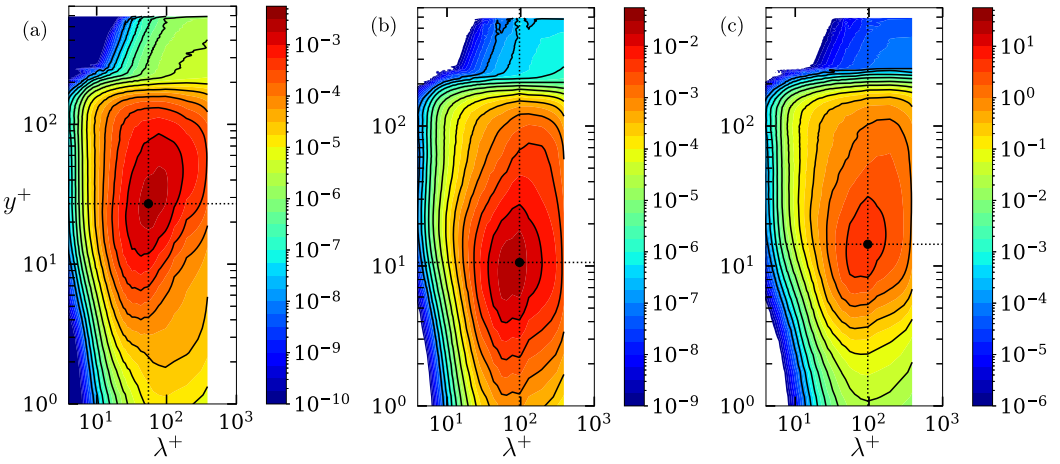

FIG. 16. Premultiplied spanwise spectra $k_z E_{vv}/u_\infty^2$ (a), $k_z E_{uu}/u_\infty^2$ (b) and $k_z E_{TT}/T_\infty^2$ (c) for the chemical nonequilibrium simulation, at $\mathrm{Re}_\tau = 185$.

and under the assumptions of (1) no-slip condition at the wall, (2) homogeneity in the spanwise direction, and (3) no body force, the mean skin friction drag coefficient can be expressed as

$$C_f = \underbrace{\frac{2}{\rho_\infty u_\infty^3}\int_0^\delta \overline{\tau}_{xy}\frac{\partial \widetilde{u}}{\partial y}\,dy}_{C_{f,1}} + \underbrace{\frac{2}{\rho_\infty u_\infty^3}\int_0^\delta -\overline{\rho u'' v''}\frac{\partial \widetilde{u}}{\partial y}\,dy}_{C_{f,2}} + \underbrace{\frac{2}{\rho_\infty u_\infty^3}\int_0^\delta (\widetilde{u}-u_\infty)\left[\overline{\rho}\left(\widetilde{u}\frac{\partial \widetilde{u}}{\partial x}+\widetilde{v}\frac{\partial \widetilde{u}}{\partial y}\right)-\frac{\partial}{\partial x}\left(\overline{\tau}_{xx}-\overline{\rho}\widetilde{u''u''}-\overline{p}\right)\right]dy}_{C_{f,3}}. \tag{28}$$

The terms denoted as $C_{f,1}$ and $C_{f,2}$ represent the contributions of the mean-field molecular dissipation and the dissipation due to the Reynolds stresses, respectively; $C_{f,3}$ accounts for the boundary layer spatial growth and includes the effects of streamwise heterogeneity. Figure 17(a) shows that the sum of the preceding terms computed from DNS data is in excellent agreement with the total skin friction coefficient, with minor discrepancies next to the suction-and-blowing forcing location. The presence of chemical reactions does not affect the validity of the decomposition, which is

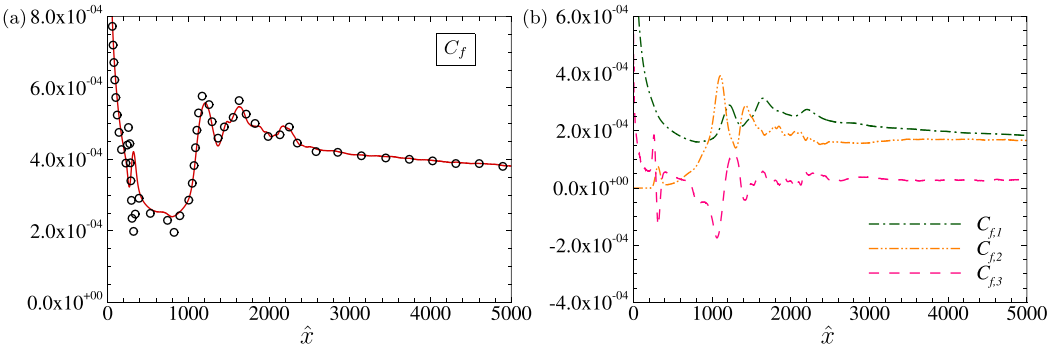

FIG. 17. Streamwise evolution of skin friction coefficient (——) superposed with Renard-Deck decomposition (symbols) (a) and contribution of each term of Eq. (28) (b) for the chemical nonequilibrium case.

derived under rather general hypotheses. In the fully turbulent region, $C_{f,1}$ and $C_{f,2}$ are preponderant with respect to the third term [Fig. 17(b)]. We also observe that $C_{f,1}$ contributes more than $C_{f,2}$, consistently with the relatively low Reynolds numbers reached at the end of the plate [58].

IV. CONCLUSIONS

A high-enthalpy hypersonic turbulent boundary layer at Mach 10, spatially developing along a quasi-adiabatic flat plate, is investigated by means of DNS. The fluid is air, modeled by using the five-species model of Park. The free-stream thermodynamic conditions are such that gas dissociation phenomena occur, giving rise to a nonequilibrium chemical state. At the considered wall temperature, oxygen and a small amount of nitrogen dissociate. The influence of such high-temperature effects on turbulence dynamics is then investigated by comparing first- and second-order flow statistics to those obtained for a turbulent boundary layer of an oxygen/nitrogen mixture with frozen chemistry.

The main effect of gas dissociation is to change the mixture composition near the wall, in the region comprised between the viscous and buffer sublayers, modifying the fluid thermo-physical properties. Additionally, the endothermic chemical reactions drain energy from the flow in the turbulence production region, leading to slightly smaller streamwise turbulent intensity and to a reduction of temperature fluctuations by approximately 10%. The small values observed for the mean Damköhler numbers of the species point out that chemical dissociation is much slower than the characteristic timescale of the flow, i.e., the flow is not far from frozen flow conditions; turbulence/chemistry interactions are thus found to be small. In this situation, the main differences with respect to a frozen flow are observed for the thermodynamic quantities; on the contrary, the presence of chemical reactions does not alter substantially velocity fluctuations or turbulent spectra. The DNS data have been used to assess some classical modeling assumptions derived from the Strong Reynolds Analogy theory. The latter is shown to remain valid, provided that corrections accounting for total temperature fluctuations are applied. The well known assumptions of a constant turbulent Prandtl number and constant turbulent Schmidt number, classically used to model turbulent transport of heat and species mass fractions, respectively, is also investigated. The results show that, while the constant Prandtl number is a rather crude one, in agreement with previous results in the literature, the constant Schmidt number is better respected, except in the immediate neighborhood of the wall were a noncatalytic condition is applied. However, the Schmidt number does not take a nearly unit value for all of the present species, and species-dependent coefficients should be adopted for better accuracy. Finally, the Renard-Deck decomposition for the skin friction coefficient has been found to remain valid also at the present severe hypersonic conditions.

The present DNS was carried out under hypothetical freestream conditions and with a quasiadiabatic wall, a canonical configuration routinely analyzed in the past for stability studies. Thermodynamic quantities downstream of a shock wave could be more representative of realistic flight conditions. This would lead to larger edge temperatures than the one considered in this study, albeit we would still expect similar qualitative behaviors in terms of turbulence/chemistry timescales separation and streamwise evolutions. More influential is the contribution of wall cooling, which is the authors' ongoing work. In that case, it is expected that the region of maximum chemical activity moves away from the wall approaching that of maximum turbulence production, thus enhancing the turbulence-chemistry interactions. Thermal nonequilibrium conditions will be considered as well, with the aim of quantifying the influence of thermal relaxation phenomena on wall turbulence dynamics.

ACKNOWLEDGMENTS

D.P. and G.P. were partially supported by the Italian Ministero dell'Istruzione, dell'Università e della Ricerca under the Programme Department of Excellence Legge 232/2016 (Grant No. CUP-D94I18000260001). The present project was granted access to the HPC resources of IDRIS

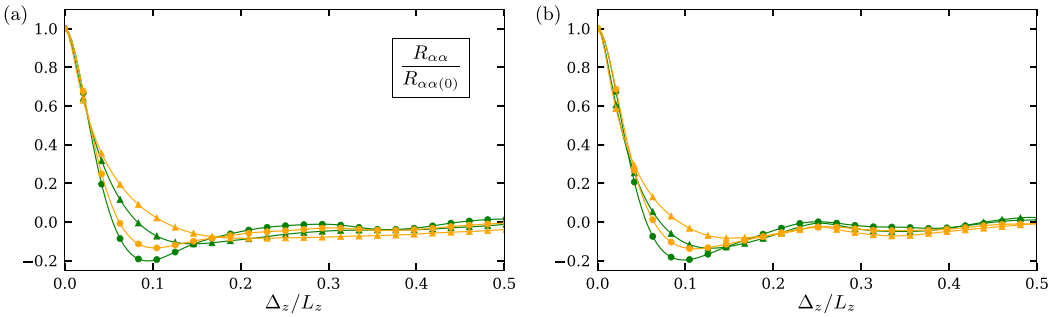

FIG. 18. Distribution of two-point correlations in the spanwise direction, at $\mathrm{Re}_\tau = 185$: $\alpha = u$, at $y^+ = 10$ (—●—) and $y^+ = 150$ (—▲—); $\alpha = \rho$, at $y^+ = 10$ (—●—) and $y^+ = 150$ (—▲—). (a) CN case; (b) FR case.

and TGCC, under the Allocation No. 2019-A0072B10947, made by GENCI (Grand Equipement National de Calcul Intensif). We also acknowledge CINECA for awarding access to the Galileo supercomputer under the Allocation No. HP10CLMXP0.

APPENDIX: ASSESSMENT OF MESH ADEQUACY

In this Appendix, additional material is provided in order to verify the adequacy of the selected computational mesh. According to Poggie *et al.* [59], the spanwise extent of the computational domain should be at least twice the local boundary layer thickness, δ_{99}, in order to ensure proper decorrelation in the spanwise direction. By considering the δ_{99} value at the end of the flat plate, we obtain for the present simulation $(L_x \times L_y \times L_z)/\delta_{99,\mathrm{end}} = 65 \times 3 \times 2$, which meets the suggested recommendation. Direct confirmation is obtained by inspection of the two-points spanwise correlations, shown in Fig. 18 for density and streamwise velocity at two different wall-normal locations (one near the turbulent production inner peak, $y^+ \approx 10$, and another in the logarithmic zone). With regard

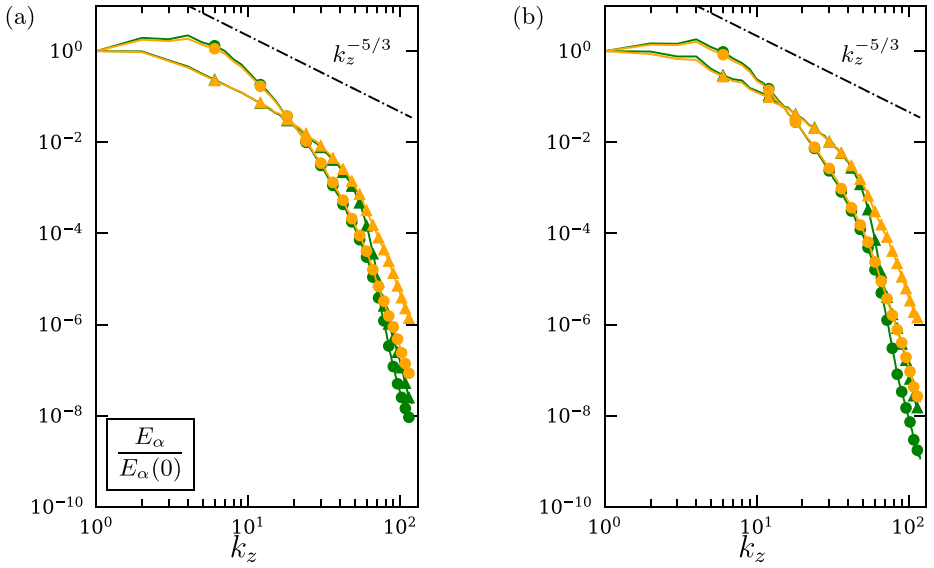

FIG. 19. One-dimensional energy spectra in the spanwise direction, at $\mathrm{Re}_\tau = 185$: $\alpha = \rho u^2$, at $y^+ = 10$ (—●—) and $y^+ = 150$ (—▲—); $\alpha = T$, at $y^+ = 10$ (—●—) and $y^+ = 150$ (—▲—). (a) CN case; (b) FR case.

to the resolution, the authors indicate that using $\Delta x^+ < 10$, $\Delta y^+ < 1$ and $\Delta z^+ < 5$ is sufficient to obtain well-converged first- and second-order statistics; resolutions shown in Table I are well below the suggested limits and ensure very accurate representation of the small details of the flow. Another important check consists in verifying the absence of energy pileup at high wave numbers; to this aim, we report the one-dimensional kinetic energy spectra in Fig. 19, at the same two wall positions. The energy distribution cascades down smoothly for approximately nine orders of magnitude, with an inertial range extending for more than a decade in the logarithmic region. The cutoff wave number indicates a good grid resolution and no energy accumulation is observed at the smallest scales.

[1] I. A. Leyva, The relentless pursuit of hypersonic flight, Phys. Today **70**(11), 30 (2017).

[2] G. Colonna, F. Bonelli, and G. Pascazio, Impact of fundamental molecular kinetics on macroscopic properties of high-enthalpy flows: The case of hypersonic atmospheric entry, Phys. Rev. Fluids **4**, 033404 (2019).

[3] G. Candler, Rate effects in hypersonic flows, Annu. Rev. Fluid Mech. **51**, 379 (2019).

[4] J. J. Bertin and R. M. Cummings, Critical hypersonic aerothermodynamic phenomena, Annu. Rev. Fluid Mech. **38**, 129 (2006).

[5] C. Roy and F. Blottner, Review and assessment of turbulence models for hypersonic flows, Prog. Aerospace Sci. **42**, 469 (2006).

[6] M. R. Malik, Stability theory for chemically reacting flows, in *Laminar-Turbulent Transition*, edited by D. Arnal and R. Michel, International Union of Theoretical and Applied Mechanics (Springer, Berlin, Heidelberg, 1990).

[7] O. Marxen, T. Magin, G. Iaccarino, and E. Shaqfeh, A high-order numerical method to study hypersonic boundary-layer instability including high-temperature gas effects, Phys. Fluids **23**, 084108 (2011).

[8] X. Zhong and X. Wang, Direct numerical simulation on the receptivity, instability, and transition of hypersonic boundary layers, Annu. Rev. Fluid Mech. **44**, 527 (2012).

[9] O. Marxen, T. E. Magin, E. Shaqfeh, and G. Iaccarino, A method for the direct numerical simulation of hypersonic boundary-layer instability with finite-rate chemistry, J. Comput. Phys. **255**, 572 (2013).

[10] O. Marxen, G. Iaccarino, and T. E. Magin, Direct numerical simulations of hypersonic boundary-layer transition with finite-rate chemistry, J. Fluid Mech. **755**, 35 (2014).

[11] N. P. Bitter and J. E. Shepherd, Stability of highly cooled hypervelocity boundary layers, J. Fluid Mech. **778**, 586 (2015).

[12] C. H. Mortensen and X. Zhong, Real-gas and surface-ablation effects on hypersonic boundary-layer instability over a blunt cone, AIAA J. **54**, 980 (2016).

[13] F. Miró Miró, E. S. Beyak, F. Pinna, and H. L. Reed, High-enthalpy models for boundary-layer stability and transition, Phys. Fluids **31**, 044101 (2019).

[14] K. L. Mack, Boundary layer stability theory, Technical Report No. 900-277, Jet Propulsion Laboratory, California Institute of Technology, Pasadena, CA, 1969.

[15] J.-C. Robinet and X. Gloerfelt, Instabilities in non-ideal fluids, J. Fluid Mech. **880**, 1 (2019).

[16] J. Franko, R. W. MacCormack, and S. K. Lele, Effects of chemistry modeling on hypersonic boundary layer linear stability prediction, in *40th Fluid Dynamics Conference and Exhibit, Chicago, Illinois* (AIAA, Reston, VA, 2010), p. 4601.

[17] L. Duan, I. Beekman, and M. P. Martín, Direct numerical simulation of hypersonic turbulent boundary layers. Part 2. Effect of wall temperature, J. Fluid Mech. **655**, 419 (2010).

[18] L. Duan, I. Beekman, and P. Martín, Direct numerical simulation of hypersonic turbulent boundary layers with varying freestream Mach number, in *48th AIAA Aerospace Sciences Meeting Including the New Horizons Forum and Aerospace Exposition* (AIAA, Reston, VA, 2010), p. 353.

[19] M. Lagha, J. Kim, J. D. Eldredge, and X. Zhong, A numerical study of compressible turbulent boundary layers, Phys. Fluids **23**, 015106 (2011).

[20] L. Duan and M. P. Martín, Direct numerical simulation of hypersonic turbulent boundary layers. Part 4. Effect of high enthalpy, J. Fluid Mech. **684**, 25 (2011).
[21] C. Zhang, L. Duan, and M. M. Choudhari, Direct numerical simulation database for supersonic and hypersonic turbulent boundary layers, AIAA J. **56**, 4297 (2018).
[22] J. Huang, G. L. Nicholson, L. Duan, M. M. Choudhari, and R. D. Bowersox, Simulation and modeling of cold-wall hypersonic turbulent boundary layers on flat plate, in *AIAA SciTech Forum, Orlando, FL* (AIAA, Reston, VA, 2020), pp. 1–23.
[23] L. Duan and M. P. Martín, Effect of finite-rate chemical reactions on turbulence in hypersonic turbulence boundary layers, in *47th AIAA Aerospace Sciences Meeting Including The New Horizons Forum and Aerospace Exposition* (AIAA, Reston, VA, 2009), p. 588.
[24] L. Duan and M. P. Martín, Assessment of turbulence-chemistry interaction in hypersonic turbulent boundary layers, AIAA J. **49**, 172 (2011).
[25] A. G. Neville, I. Nompelis, P. K. Subbareddy, and G. V. Candler, Effect of thermal non-equilibrium on decaying isotropic turbulence, in *Proceedings of the 7th AIAA Theoretical Fluid Mechanics Conference* (AIAA, Atlanta, GA, 2014) p. 3204.
[26] S. Khurshid and D. A. Donzis, Decaying compressible turbulence with thermal non-equilibrium, Phys. Fluids **31**, 015103 (2019).
[27] A. G. Neville, I. Nompelis, P. K. Subbareddy, and G. V. Candler, Thermal non-equilibrium effects in turbulent compressible shear flows, in *45th AIAA Fluid Dynamics Conference* (AIAA, Reston, VA, 2015), p. 3218.
[28] M. R. Malik and E. C. Anderson, Real gas effects on hypersonic boundary-layer stability, Phys. Fluids A **3**, 803 (1991).
[29] M. L. Hudson, N. Chokani, and G. V. Candler, Linear stability of hypersonic flow in thermochemical nonequilibrium, AIAA J. **35**, 958 (1997).
[30] J. Perraud, D. Arnal, L. Dussillols, and F. Thivet, Studies of laminar-turbulent transition in hypersonic boundary layers at ONERA, in *Third European Symposium on Aerothermodynamics for Space Vehicle*, Vol. 426 (Noordwijk, The Netherlands, 1998), p. 309.
[31] F. Miró Miró, F. Pinna, E. S. Beyak, P. Barbante, and H. L. Reed, Diffusion and chemical non-equilibrium effects on hypersonic boundary-layer stability, in *2018 AIAA Aerospace Sciences Meeting* (AIAA, Reston, VA, 2018), p. 1824.
[32] P. A. Gnoffo, R. N. Gupta, and J. L. Shinn, Conservation equations and physical models for hypersonic air flows in thermal and chemical nonequilibrium, Technical Report No. N-89-16115, Langley Research Center, National Aeronautics and Space Administration, Hampton, VA, USA, 1989.
[33] C. Park, *Nonequilibrium Hypersonic Aerothermodynamics* (John Wiley & Sons, 1990).
[34] F. G. Blottner, M. Johnson, and M. Ellis, Chemically reacting viscous flow program for multi-component gas mixtures, Technical Report No. SC-RR-70-754, Sandia Labs., Albuquerque, N. Mexico, Livermore, California, 1971.
[35] T. E. Magin and G. Degrez, Transport algorithms for partially ionized and unmagnetized plasmas, J. Comput. Phys. **198**, 424 (2004).
[36] I. Armenise, M. Barbato, M. Capitelli, and E. Kustova, State-to-state catalytic models, kinetics, and transport in hypersonic boundary layers, J. Thermophys. Heat Transfer **20**, 465 (2006).
[37] S. Subramaniam, R. L. Jaffe, and K. A. Stephani, State-resolved transport collision integrals for the $O + O_2$ system, Phys. Rev. Fluids **5**, 113402 (2020).
[38] T. Poinsot and D. Veynante, *Theoretical and Numerical Combustion* (R. T. Edwards, Philadelphia, PA, 2005).
[39] V. Giovangigli, Multicomponent flow modeling, Sci. China Math. **55**, 285 (2012).
[40] J. O. Hirschfelder, C. F. Curtiss, R. B. Bird, and M. G Mayer, *Molecular Theory of Gases and Liquids* (Wiley, New York, 1964), Vol. 165.
[41] R. N. Gupta, J. M. Yos, and K. P. Lee, A review of reaction rates and thermodynamic and transport properties for an 11-species air model for chemical and thermal nonequilibrium calculations to 30000 K, Technical Report No. N-89-21193, NASA, USA, 1989.

[42] C. Park, Review of chemical-kinetic problems of future NASA missions. I—Earth entries, J. Thermophys. Heat Transfer **7**, 385 (1993).
[43] M. Panesi, R. L. Jaffe, D. W. Schwenke, and T. E. Magin, Rovibrational internal energy transfer and dissociation of $N_2(^1\Sigma_g^+) - N(^4S_u)$ system in hypersonic flows, J. Chem. Phys. **138**, 044312 (2013).
[44] S. Venturi, M. P. Sharma, B. Lopez, and M. Panesi, Data-inspired and physics-driven model reduction for dissociation: Application to the O_2+ O system, J. Phys. Chem. A **124**, 8359 (2020).
[45] A. Cook and W. Cabot, A high-wavenumber viscosity for high-resolution numerical method, J. Comput. Phys. **195**, 594 (2004).
[46] S. Kawai, K. Santhosh, and S. K. Lele, Assessment of localized artificial diffusivity scheme for large-eddy simulation of compressible turbulent flows, J. Comput. Phys. **229**, 1739 (2010).
[47] S. Gottlieb and C.-W. Shu, Total variation diminishing Runge-Kutta schemes, Math. Comput. **67**, 73 (1998).
[48] T. J. Poinsot and S. K. Lele, Boundary conditions for direct simulations of compressible viscous flows, J. Comput. Phys. **101**, 104 (1992).
[49] H. M. Nagib and K. A. Chauhan, Variations of von Kármán coefficient in canonical flows, Phys. Fluids **20**, 101518 (2008).
[50] P. A. Monkewitz, Revisiting the quest for a universal log-law and the role of pressure gradient in canonical wall-bounded turbulent flows, Phys. Rev. Fluids **2**, 094602 (2017).
[51] M. V. Morkovin, Effects of compressibility on turbulent flows, in *Mécanique de la turbulence*, edited by A. Favre (CNRS, Paris, 1962), pp. 367-380.
[52] S. E. Guarini, R. D. Moser, K. Shariff, and A. Wray, Direct numerical simulation of a supersonic turbulent boundary layer at Mach 2.5, J. Fluid Mech. **414**, 1 (2000).
[53] P. G. Huang, G. N. Coleman, and P. Bradshaw, Compressible turbulent channel flows: DNS results and modelling, J. Fluid Mech. **305**, 185 (1995).
[54] L. Duan, I. Beekman, and M. P. Martín, Direct numerical simulation of hypersonic turbulent boundary layers. Part 3. Effect of Mach number, J. Fluid Mech. **672**, 245 (2011).
[55] L. Sciacovelli, X. Gloerfelt, D. Passiatore, P. Cinnella, and F. Grasso, Numerical investigation of high-speed turbulent boundary layers of dense gases, Flow, Turbul. Combust. **105**, 555 (2020).
[56] N. Renard and S. Deck, A theoretical decomposition of mean skin friction generation into physical phenomena across the boundary layer, J. Fluid Mech. **790**, 339 (2016).
[57] W. Li, Y. Fan, D. Modesti, and C. Cheng, Decomposition of the mean skin-friction drag in compressible turbulent channel flows, J. Fluid Mech. **875**, 101 (2019).
[58] Y. Fan, W. Li, and S. Pirozzoli, Decomposition of the mean friction drag in zero-pressure-gradient turbulent boundary layers, Phys. Fluids **31**, 086105 (2019).
[59] J. Poggie, N. J. Bisek, and R. Gosse, Resolution effects in compressible, turbulent boundary layer simulations, Comput. Fluids **120**, 57 (2015).